Mechanical Systems and Signal Processing 257 (2026) 114615

Contents lists available at ScienceDirect

Mechanical Systems and Signal Processing

journal homepage: www.elsevier.com/locate/ymssp

Full Length Article

Approximation of structural intensity from experimental structural response data using a hybrid method – methodology, verification, and validation

Sebastian F. Zettel [a,b,*], René Winter [a], Marc Böswald [a], Marcus Maeder [b], Steffen Marburg [b]

[a] German Aerospace Center (DLR), Institute of Aeroelasticity, Germany
[b] Chair of Vibroacoustics of Vehicles and Machines, TUM School of Engineering and Design, Germany

ARTICLE INFO

Keywords:
Structural intensity
Power flow analysis
Structural response

ABSTRACT

Structural intensity is a response quantity that allows visualization and quantification of the vibrational power flow in structures. Numerical simulations allow for easy calculation, i.e., by combining standard result datasets of finite element analysis. However, this is not the case for experimental data, where usually an incomplete set of response quantities (i.e., just translational responses) of a subset of the degrees of freedom of the corresponding finite element model serves as the fundamental dataset to compute the structural intensity. This paper provides a comprehensive guide for a hybrid method that allows the calculation of structural intensity on arbitrary surfaces in three-dimensional space. The hybrid method utilizes experimentally acquired structural response data as an input. The corresponding measurement point locations build a mesh with associated trial functions. Furthermore, a verification of the methodology utilizing numerical data to quantify the method's accuracy is performed. Moreover, comparing structural intensity fields acquired from a numerical model and measurement data helps to validate the proposed approach further. Finally, the methodology supports engineers and researchers in utilizing the concept of structural intensity to optimize mechanical systems in terms of structural dynamics, e.g., the smart application of damping elements to control system dynamics efficiently.

1. Introduction

Structural intensity (STI) allows visualization and quantification of the vibrational power flow in structures. This analysis is possible by calculating STI vectors from structural response data evaluated for a finite number of discrete locations. Multiplying the local stress tensor by the local vibration velocity response vector yields the local STI vectors. These local STI vectors indicate the direction and magnitude of the power flow at the corresponding locations. A specific postprocessing method, i.e., vector field decomposition, allows the identification of sources and sinks of vibrations in these STI vector fields. Ideally, this enables the efficient placement of countermeasures for vibration reduction.

Since the first papers on the STI topic in the 1970 s, research has focused on approximating vector fields from measurement data. Researchers have applied state-of-the-art measurement techniques used in vibration and acoustics, such as accelerometers [1–5], laser

* Corresponding author at: Bunsenstraße 10, 37073 Göttingen, Germany.
E-mail address: sebastian.zettel@dlr.de (S.F. Zettel).

https://doi.org/10.1016/j.ymssp.2026.114615
Received 29 October 2025; Received in revised form 11 February 2026; Accepted 23 June 2026
Available online 27 June 2026
0888-3270/

Doppler vibrometers (LDVs) [6–9], acoustic holography [10,11], and digital image correlation [12–14]. These measurement techniques allow the acquisition of deformation or velocity fields on the surface of structures. Thin-walled structures or beam-like structures, such as plates, beams, and pipes, are prone to vibrations and are therefore the main subject of investigation. The STI flow in the thickness direction has been neglected because of the assumption that the acquired responses on the surface are constant over the structure's thickness for thin-walled structures. With respect to plate-like structures, the required stresses are approximated via plate constitutive equations according to Kirchhoff (classical plate theory) [15] or Mindlin–Reissner plate theory [15], assuming known material properties and known geometric shapes. The focus of investigations is not only on simple academic structures but also on more complex but still thin-walled structures. Investigations have been performed on structures in engineering fields with a high focus on noise reduction for passenger comfort, such as automotive applications [16–18] and aerospace applications [19–22]. Additionally, investigations focused on damage detection are ongoing [23–25].

Pavic et al. [2] have formulated the eight-sensor method, which is a commonly used approach to solve the plate equation for missing stresses to calculate the STI. This method uses the finite difference method for calculating derivatives. The *eight-sensor method* has the drawback of not being generally applicable to arbitrary surfaces. In the case of curved surfaces, e.g., cylinders, the shell equations require an adaptation to the given coordinate system via a curved-linear implementation [26]. This circumstance increases the difficulty of evaluating structures, especially for arbitrarily shaped surfaces in three-dimensional space (2-manifolds). Therefore, a general methodology is necessary that allows the calculation of the STI on the basis of response data of arbitrarily shaped surfaces.

In 2018, Biedermann et al. [20] have presented an approach that uses finite element method (FEM) theory to calculate the missing data required for the STI calculation from experimentally acquired response data. The basic idea is to combine experimental responses with approaches from the FEM. The approach uses measured structural response data at discrete measurement points as input. Furthermore, the measurement points are regarded as the nodes of an FEM-like mesh. Bilinear shape functions for four-node shell elements are set up to calculate nodal rotations at the nodes of the element and forces, as well as moments in the centroid of the element. Compared with the previously mentioned finite difference method, the use of four-node shell elements allows the calculation of STI vectors with a subset of measurement points. Owing to the utilized FEM approach, this method also allows a direct comparison at the node and element levels to respective evaluations with an FEM model. Considering that researchers usually use numerical and experimental approaches in synergy, this is a significant advantage when considering the updating procedure of finite element (FE) models. The results of Biedermann et al. [20] look promising but lack a detailed evaluation of the method's accuracy regarding the approximated data, i.e., nodal rotations and elemental forces and moments. Additionally, an exhaustive description of the methodology, including the FEM approach, is missing. Pires et al. [12] have published an approach similar to that of Biedermann et al. that uses six-node triangular shell elements. Six-node elements—and, more generally, elements with mid-edge nodes—allow the use of quadratic shape functions, which provide a clear advantage. They allow the computation of transversal forces with high accuracy because two consecutive derivatives can be performed. However, such accurate transversal forces are needed only when the conditions for moderately thick plates, as defined by Mindlin [27], are met. The hybrid method focuses on efficiently analyzing thin-walled structures. For this reason, four-node elements are used in this work because they allow STI vectors to be computed efficiently while aiming to reduce measurement effort in large-scale structures.

Building on the *hybrid method* concept introduced by Biedermann et al. [20], this work provides a comprehensive description and verification of the methodology. Furthermore, a validation of the approach is performed through experiments on a laboratory structure. The hybrid method combines experimental structural response data with the FEM approach for calculating elemental forces and moments. In this work, four-node quadrilateral shell elements are used, as they can acquire the necessary internal element forces via Kirchhoff plate theory with a low number of nodes. The reason is the chosen thin-walled geometry used for the numerical model and the equivalent experimental structure. Furthermore, this paper covers a detailed verification of the hybrid method. This concept includes an evaluation of the accuracy of the approximated nodal rotations and the elemental forces and moments in comparison to a ground truth FEM dataset. The hybrid method is subsequently applied to experimentally acquired structural response data of a plate structure. The STI vector field calculated from the measurement data is compared to a set of STI vector fields acquired from a numerical FE model representing the experimental structure. Afterwards, the vector fields are compared qualitatively, in terms of their flow characteristics, and quantitatively, in terms of their magnitudes.

The paper is organized as follows: Section 2 describes the fundamentals of structural intensity and the basic approach for calculating the respective vectors. Section 3 outlines the hybrid method, which allows the calculation of the STI from measurement data. Section 4 covers the verification of the hybrid method. The hybrid method's accuracy is quantified by comparing the STI calculated with a full FE dataset to a dataset based on the same FE dataset but using only its nodal translatory response data. Section 5 covers the comparison of experimentally and numerically acquired STI vector fields. The paper closes with a section stating a conclusion and an outlook containing suggestions for developments to further improve the hybrid method.

2. Fundamentals of structural intensity

The structural intensity (STI) describes the vibrational power flow per cross-sectional area in a structure as a vector. The STI is related to the concept of sound intensity, which quantifies the magnitude and direction of energy radiated by a sound source in a fluid such as air. The instantaneous sound intensity is calculated with the scalar pressure p and the particle velocity vector $\overrightarrow{\mathrm{v}}$ in the time-domain [28]. In the subsequent outlines, subscripts t and f denote the functional dependency on time and frequency, respectively. In the case of the STI, the scalar pressure value is replaced with the stress tensor S for a solid material [28]; see Fig. 2.1. Therefore, the instantaneous STI vector $\overrightarrow{\mathrm{I}}$ at an arbitrary point in a solid is calculated by

$$\vec{I}_{solid,t} = -S\begin{bmatrix} v_x \\ v_y \\ v_z \end{bmatrix} = -\begin{bmatrix} \sigma_x & \tau_{xy} & \tau_{xz} \\ \tau_{yx} & \sigma_y & \tau_{yz} \\ \tau_{zx} & \tau_{zy} & \sigma_z \end{bmatrix}\begin{bmatrix} v_x \\ v_y \\ v_z \end{bmatrix} \tag{2.1}$$

where the normal stress σ and the shear stress τ [28]. The negation is necessary because the stress convention describes compression with negative values.

The following time-dependence of the harmonic vibrations is considered by

$$u(t) = \mathrm{Re}\left\{\underline{u}\exp(j\,2\pi f\,t)\right\} \tag{2.2}$$

with the complex displacement $\underline{u}$, the imaginary unit j, the frequency f and the time t. The expression Re{ • } describes the real part of a complex number. The complex displacement is described by

$$\underline{u} = \hat{u}\exp(j\phi) \tag{2.3}$$

with the displacement amplitude $\hat{u}$ and the phase ϕ.

Acquiring the full stress and velocity fields of relevant structures built up from full material is almost impossible with the standard measurement techniques used in acoustics and vibration. Therefore, the STI is commonly used to assess the vibroacoustic behavior of thin-walled structures, and plate or shell elements are used mainly in FEM analyses [30]. In the case of thin-walled structures, the z-components of the stress tensor in Eq. (21) are neglected and set to zero (see Fig. 8.1 in the Appendix as a reference for internal loads in thin-walled structures). This simplification allows flexural deformations of the structure, which lead to bending moments that require inclusion in the description. The instantaneous power flow P for plate-like structures, i.e., quadrilateral plate elements in the FEM, is calculated by using the normal forces N, the transverse shear forces Q and the moments M in combination with the structural response in the form of velocities and the respective angular velocities ω [31] by

$$\vec{P}_{plate,t} = -\left\{\begin{bmatrix} N_x & N_{xy} & Q_{xz} \\ N_{yx} & N_y & Q_{yz} \\ 0 & 0 & 0 \end{bmatrix}\begin{bmatrix} v_x \\ v_y \\ v_z \end{bmatrix} + \begin{bmatrix} M_{xy} & M_x & 0 \\ M_y & M_{yx} & 0 \\ 0 & 0 & 0 \end{bmatrix}\begin{bmatrix} \omega_x \\ \omega_y \\ \omega_z \end{bmatrix}\right\} \tag{2.4}$$

The forces and moments are assumed to act in the element centroid. Any relevant values defined only at the nodes, i.e., translatory velocity and angular velocity, must be mapped to the element center. For regular FE meshes, this step can be carried out by simply averaging the nodal values associated with the element. In the case of irregular meshes, a more appropriate method is necessary, e.g., the shape function approach (see Eq. (8.22) through Eq. (8.25) in the Appendix as a reference).

Considering the harmonic excitation of a damped structure, the response is assumed to reach steady-state behavior after a finite time. Accordingly, the time-averaged STI in the frequency-domain is acquired by using the complex frequency-domain values of the forces, moments, velocities, and angular velocities

$$\vec{\underline{I}}_{plate,f} = -\frac{1}{2A}\left\{\begin{bmatrix} \underline{N}_x & \underline{N}_{xy} & \underline{Q}_{xz} \\ \underline{N}_{yx} & \underline{N}_y & \underline{Q}_{yz} \\ 0 & 0 & 0 \end{bmatrix}\begin{bmatrix} \underline{v}_x^* \\ \underline{v}_y^* \\ \underline{v}_z^* \end{bmatrix} + \begin{bmatrix} \underline{M}_{xy} & \underline{M}_x & 0 \\ \underline{M}_y & \underline{M}_{yx} & 0 \\ 0 & 0 & 0 \end{bmatrix}\begin{bmatrix} \underline{\omega}_x^* \\ \underline{\omega}_y^* \\ \underline{\omega}_z^* \end{bmatrix}\right\} \tag{2.5}$$

where A is the cross-sectional area in the flow direction that transforms the power flow into an intensity, the asterisk superscript indicates complex conjugate values, and the underscore indicates complex values.

The real part of the STI is the so-called *active* part of the energy or power flow. It is the part of the energy that forms a flow throughout a structure and is ultimately dissipated. The imaginary part on the other side is the *reactive* part and describes the exchange of potential and kinetic energy. The active and reactive parts of the STIs are related to the respective active and reactive powers known from electrodynamic theory. Maysenhölder [32] has conducted a comprehensive investigation of the reactive STI. According to his investigation, one can describe the sources and sinks of the reactive STI by the mean time-averaged difference in kinetic and potential energy. Imaginary power emerges in regions where the time-averaged mean kinetic energy exceeds the respective potential energy and

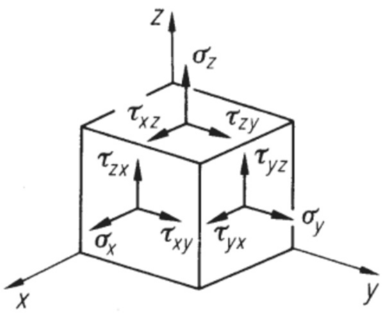

Fig. 2.1. Stress tensor in the 3D orthogonal coordinate system [29].

vanishes for prevailing potential energy. Overall, the energy is conserved. Maysenhölder has stated that the reactive part of airborne wavefields allows the energy flow density to be calculated as a function of time, the time average of the Lagrangian density, and the rotational part of the active STI. However, he has concluded that the mentioned benefits do not apply to structure-borne wavefields. Importantly, the active part can only emerge for existing damping or any effect that results in a phase shift between the excitation and the structural response. This circumstance is described with an instantaneous power injection into a structure by [32]

$$P_{\mathrm{in,t}} = Fv = \mathrm{Re}\left\{\underline{F}\exp(j\,2\pi f\,t)\right\}\mathrm{Re}\left\{\underline{v}\exp(j\,2\pi f\,t)\right\} \tag{2.6}$$

with the complex representations $\underline{F} = \widehat{F}\exp(j\phi)$ and $\underline{v} = \widehat{v}\exp(j\psi)$ of a harmonic point force F and the driving point velocity v. The values with a roof on top describe the amplitudes, and ϕ and ψ are the respective phases. By including the complex representations of force and velocity in Eq. (2.6) and considering a harmonic excitation with a cosine character, the injected power is described by [32]

$$P_{\mathrm{in,t}} = \frac{1}{2}\widehat{F}\,\widehat{v}\left[\cos(\phi+\psi+4\pi f\,t)+\cos(\phi-\psi)\right] \tag{2.7}$$

Accordingly, the time-averaged injected power is represented by [32]

$$P_{\mathrm{in,f}} = \frac{1}{2}\widehat{F}\,\widehat{v}\cos(\phi-\psi) = \frac{1}{2}\widehat{F}\,\widehat{v}\mathrm{Re}\{\exp(j(\phi-\psi)\} = \frac{1}{2}\mathrm{Re}\left\{\underline{F}\,\underline{v}^{*}\right\}. \tag{2.8}$$

Only for $(\phi-\psi) \neq (2n-1)\frac{\pi}{2}$ with $n \in \mathbb{N}$ is power injected into the system [33]. The phase shift between $\widehat{F}$ and $\widehat{v}$ is induced by any damping mechanism or a combination of these, i.e., material damping, a local dashpot damper, acoustic radiation, or an actively controlled mechanism that attenuates the system's response at a local point. An ideal phase shift of $(\phi-\psi) = (2n-1)\frac{\pi}{2}$ occurs for nonexistent damping at a resonance. In this case, only a reactive STI is present in the system [32].

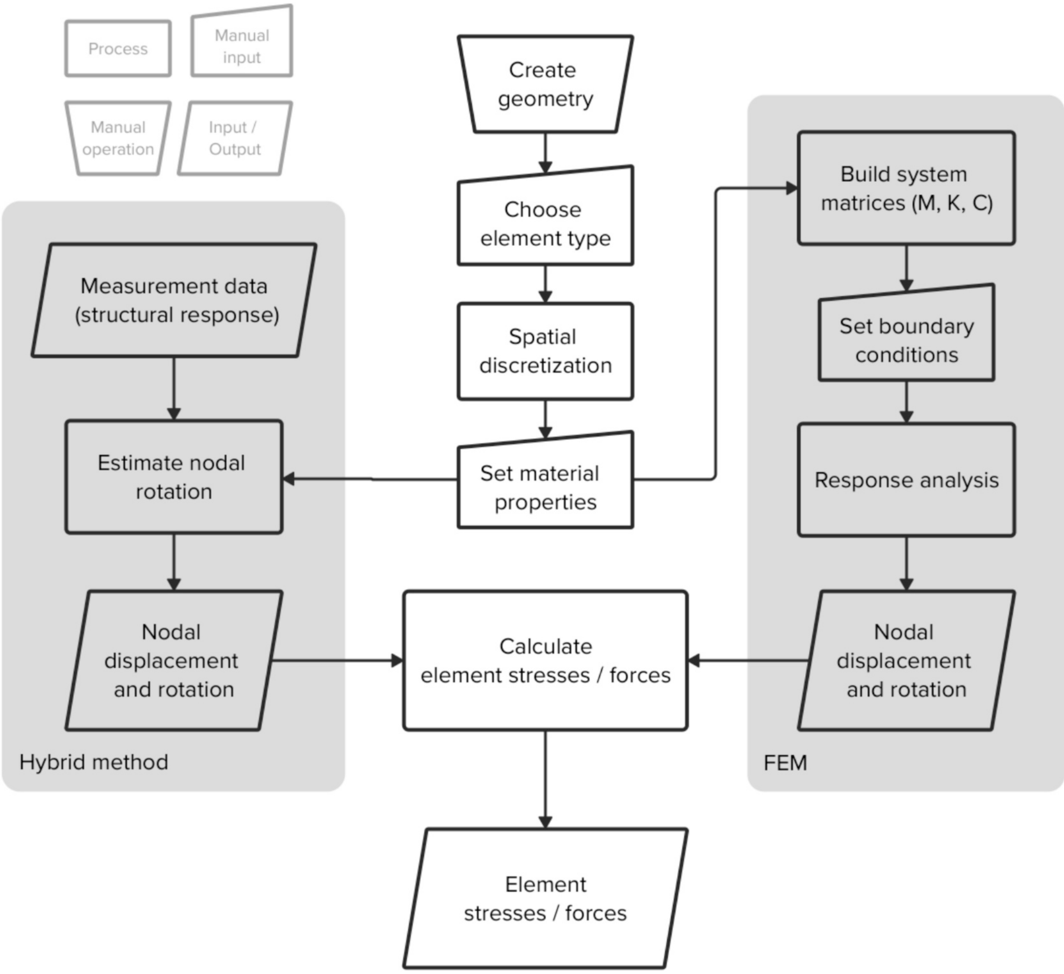

Fig. 3.1. Overview of the sequential steps of the FEM and the hybrid method process chain.

Considering Eq. (2.5), one can easily calculate the STI for FE models, as all necessary data are available as a result of the simulation. The completeness of results is usually unavailable for experimental investigations of structures. With common experimental methods in acoustics and vibration, i.e., accelerometers, LDVs, and digital image correlation, one can only directly acquire the translatory velocity components on the surface of structures. Estimating angular velocity components or stresses is theoretically possible, but the measurement is only possible with disproportionate effort. Hence, the missing values require approximation. The approach to approximate the missing information is covered in the following section.

3. Hybrid method for structural intensity analysis

The fundamental idea of the proposed approximation method is to utilize the FE approach for calculating element stresses and forces on the basis of shape functions applied to measured responses from discrete measurement degrees of freedom. The flow chart in Fig. 3.1 describes both branches of the process chain: the analysis method, which is purely based on simulated responses, and the FEM and the proposed approximation methods, which use experimental data and the FE approach for the estimation of missing responses. The FEM process chain includes model generation with the building of system matrices and solving the respective equations of motion. The approximation process, however, uses measured structural response data, i.e., displacement, acceleration, and velocity fields, and the estimation of nodal rotation to acquire the desired element stresses and forces.

The approximation of nodal displacements and rotations within the hybrid method is a linear analysis step to obtain the desired results, as a subset of the nodal response data already exist from the measurements. A mesh with desired shell elements using either linear or quadratic shape functions, i.e., triangular, quadrilateral, eight- or nine-node elements, is created for the set of nodes used to acquire the measurement data. Afterwards, the required shape functions are set up for the respective mesh. Combined with the known material properties and the assumed plate theory, e.g., Kirchhoff or Mindlin-Reissner, this allows the calculation of the element forces and stresses. In general, one can consider elements with quadratic shape functions to increase the accuracy in terms of transverse forces. The reason is that a quadratic shape function allows for two consecutive derivatives. However, transverse forces are only eligible for consideration when the conditions for moderately thick plates are met [27]. Therefore, four-node elements should result in similar results when fewer nodes are used.

The measurement data captured via the LDV are initially available in the time-domain. According to the description of the hybrid method, frequency-domain data is needed. Therefore, transforming the time-domain data into frequency-domain data is necessary. One advantage of frequency-domain data is the possibility of easily transforming between velocity and displacement values at discrete frequencies by using

$$\underline{\mathrm{u}}\,(\mathrm{f}) = \frac{\underline{\mathrm{v}}\,(\mathrm{f})}{\mathrm{j}\,2\pi\mathrm{f}} \tag{3.1}$$

where the complex velocity $\underline{\mathrm{v}}$, the complex displacement $\underline{\mathrm{u}}$, the frequency f, and the imaginary unit j assemble this relation [34]. This calculation is necessary to acquire displacement values for the force and moment calculation and the nodal rotation approximation.

In the Appendix (Section 6.1), the equations Eqs. 8.1–8.28 describe the analysis of element stresses, forces, and moments for four-node quadrilateral plate elements. Plate elements use the Mindlin–Reissner plate theory, which includes transverse shear forces considering moderately thick plates. According to Mindlin [27], moderately thick plates are present when the existing wavelengths in the structure become shorter than five to ten times the plate thickness. The equations in Section 8 describing the Mindlin–Reissner plate theory also hold for the Kirchhoff plate theory when the transverse shear forces Q are neglected.

FEM calculations provide nodal displacement and rotations, on which the element forces and moments are calculated. In the case of the hybrid method, only measurement data for translational degrees of freedom are available, and nodal rotations are missing. When acceleration sensors are used for response measurements, the mesh grid of the experimental response degrees of freedom is typically

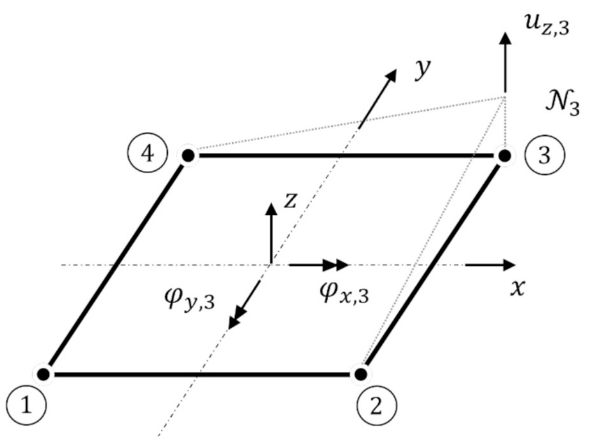

Fig. 3.2. Exemplary calculation of nodal rotation based on shape functions and nodal displacements.

coarser than that of a finite element model. However, a reasonably fine mesh resolution is possible with automated optical response measurement systems, such as LDVs.

The missing nodal rotations about the x- and y-axes, which are necessary to calculate the strains in Eq. (8.20) and Eq. (8.21) (see Appendix), are calculated via the partial differentials from Eq. (8.27) and the nodal displacements in the z-direction u_z via

$$\underline{\varphi}_{x,\,elm} = \frac{\partial u_z}{\partial y} = \left\{ \frac{\partial N_1}{\partial y} \quad \cdots \quad \frac{\partial N_4}{\partial y} \right\} \left\{ \underline{u}_{z,1} \quad \cdots \quad \underline{u}_{z,4} \right\}^T \tag{3.2}$$

$$\underline{\varphi}_{y,elm} = -\frac{\partial u_z}{\partial x} = \left\{ -\frac{\partial N_1}{\partial x} \quad \cdots \quad -\frac{\partial N_4}{\partial x} \right\} \left\{ \underline{u}_{z,1} \quad \cdots \quad \underline{u}_{z,4} \right\}^T \tag{3.3}$$

The basic idea of the nodal rotation approximation is to utilize the known shape functions N_1 to N_4 and their partial derivatives and the known nodal displacements in the normal direction of the element. The elemental rotations about the x- and y-axes are the weighted sums of the individual rotation contributions of the participating nodes one through four. In Fig. 3.2, an example for calculating the nodal rotation in radians about the y-axis with the rotation contribution of the displacement of node three is shown.

The individual rotation contribution $\varphi_{y,3}$ based on the displacement of node three in Fig. 3.2 according to Eq. 3.4 is $\underline{\varphi}_{y,3} = -\partial N_3 / \partial x \bullet \underline{u}_{z,3}$. The negation is necessary according to the conventions for the coordinate directions.

In general, every node is connected to more than one element. To obtain a continuous field of nodal rotations throughout the model, the calculated elemental rotations require averaging at every node, considering the adjacent elements. In the frequency-domain, the elemental rotations are complex values. Therefore, an averaging is performed by calculating the mean value of the summed elemental rotations participating at a node by

$$\underline{\varphi}_{node} = \frac{1}{N} \sum_{n=1}^{N} \underline{\varphi}_{n,element} \tag{3.5}$$

where $\underline{\varphi}_n$ represents the complex elemental rotations in the centroid about the x- or y-axis and N represents the number of summarized values at the investigated node for the respective direction. The nodal rotation values are necessary to calculate the strains for bending moments and transverse shear in the respective elements. The calculation of the STI vectors is performed in the element centroids; therefore, elemental rotations about the x- and y-axes are required at these positions, which are acquired directly by Eq. (3.2) and Eq. (3.3). In addition to the force and moment calculations, the availability of the rotations at the nodes allows a direct comparison of the nodal rotations between the FEM results and the approximated results from the experimental data. Notably, the averaging itself introduces an error to the nodal rotation. This topic is covered in more detail in the verification in chapter 4.1.

4. Verification of the hybrid method

The hybrid method proposed in Section 3 allows the approximation of missing response data for calculating structural intensity vectors according to Eq. (2.5). The data required to perform this approximation are the translational components of the nodal responses; the geometry data, such as the coordinates of the nodal response points and the plate thickness; and the fundamental law of elasticity of the plate material. This material law may include only a few parameters, such as the Young's modulus, shear modulus, Poisson's ratio, and density, in the case of isotropic materials following Hooke’s Law, e.g., aluminum, steel, or titanium. In the case of composite materials, the properties of multiple layers are compromised via laminate theory into an orthotropic material law. This section presents a verification of the method, which utilizes two datasets. The first dataset consists of FEM simulation results for a plate

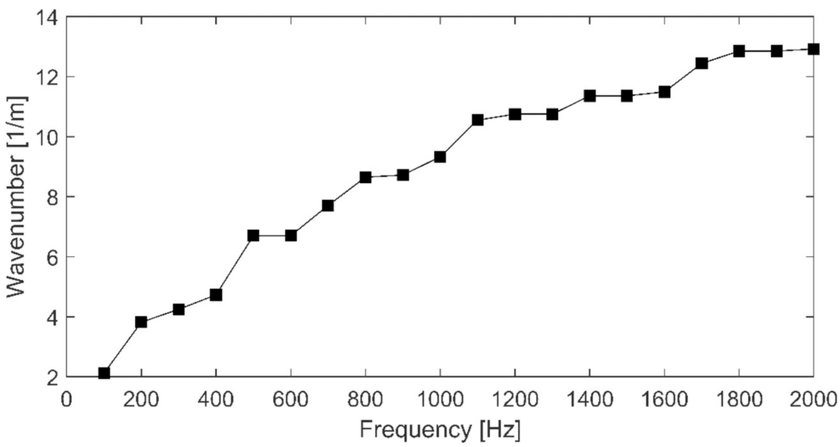

Fig. 4.1. Wavenumber over frequency of the utilized plate FE model.

structure. This dataset contains all the necessary information to calculate STI vectors, including translational and rotational nodal responses and element forces and moments in the centroids of the elements. The FEM dataset is referred to as the 'reference dataset' in the following subsections. The second dataset is based on the same FEM dataset, but only the translational nodal responses are used. Therefore, the second dataset, referred to as the 'reduced dataset', only contains data that can be obtained from a structural response measurement of a plate in an experiment. In this case, the available quantities are v_x, v_y and v_z, assuming that an LDV is used to measure the structural response. The nodal rotations as well as the elemental forces and moments require an approximation for the reduced dataset. A comparison of the approximated data in the reduced dataset and the respective data in the reference dataset allows one to quantify the accuracy of the hybrid method. This validation is performed by using relative errors for the rotational nodal data, the elemental force and moment data, and the resulting STI vector fields. The FE model represents a simple rectangular plate with dimensions of 450 mm × 300 mm in the x- and y-directions, respectively, with clamped edges. A mesh with a node spacing of 12.5 mm in both plane directions is used. A mesh density is chosen that allows accurate simulation of the structural response up to 2000 Hz. The calculation is based on a wavenumber analysis under the assumption that six linear elements per wavelength are sufficient to capture the structural response properly [35]. An FE model of the plate with a node spacing of 5 mm is the basis for creating the wavenumber over frequency in Fig. 4.1. Because of the maximum wavenumber of 13 m^{-1}, the conditions for moderately thick plates have not been met according to Mindlin [27] (see Section 3). The material properties of aluminum are used, considering Hooke's law of linear elasticity, for the FEM model with $E = 71.4$ GPa, $\rho = 2660\ \frac{kg}{m^3}$, and $\nu = 0.34$. The plate thickness is $t = 1$ mm. The plate is excited in the lower right corner (location: $x = 337.5$ mm, $y = 75$ mm) with a point force of unit magnitude $\widehat{F}_{exc} = 1$ N, having equal components in all three directions $F_{exc} = [0.577N_x, 0.577N_y, 0.577N_z]$. The excitation in all three directions allows the generation of the relevant wave types, i.e., in-plane and bending. A global stiffness proportional structural material damping of $G = 0.005$ [36] is specified. This means that the damping physically takes place in the elements, whereas the equivalent modal viscous damping is approximately 0.25% for all eigenvectors of the plate.

Additionally, a local dissipation sink is included in the FE model in the form of a dashpot damper (location: $x = 112.5$ mm, $y = 225$ mm) with a viscous damping of $d = 20$ Ns/m marked by the circle in Fig. 4.2. This source–sink pair is meant to introduce visible paths in the STI vector field in the structure that flows from source to sink. According to Eq. (2.8), a shaker only injects active power into a structure for a nonzero phase shift between the excitation force and structural response. Therefore, damping is necessary for an active STI field to emerge. However, modeling damping is a complex topic, and modeling it accurately for a wide frequency range is difficult even for a simple plate. Therefore, emerging STI fields are difficult to compare when numerical and experimental data are considered. The use of a discrete point of damping follows the idea of introducing a discrete location with increased damping to enforce the formation of distinctive paths with a well-known source and sink. Ideally, this should help to validate the hybrid method because it is easier to identify characteristics in the emerging STI vector field.

Throughout the following subsections, the relative error ε_{rel} of quantities q is calculated via

$$\varepsilon_{rel} = \frac{\left|q_{red} - q_{ref}\right|}{q_{ref}} \tag{4.1}$$

where q_{ref} and q_{red} specify the quantities of the reference and reduced datasets, respectively. The errors are presented as the median of the nodal and elemental error values per frequency line. The application of the median allows a robust view of the errors without distorting the overall relative error per frequency due to outliers.

4.1. Approximation of nodal rotation data

The relative error over the frequency of the nodal rotation approximation about the x- and y-axes is presented in Fig. 4.3. The complex nodal rotation is split into magnitude and phase to show both errors. The relative magnitude error is linearly dependent over the investigated frequency range, resulting in a maximum error of approximately 25% at 1980 Hz. The linear increase in the error is also apparent with the phase. However, the overall relative errors are two orders of magnitude lower than the magnitude, showing that

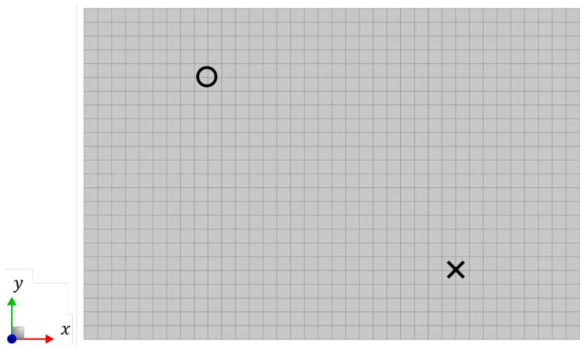

Fig. 4.2. FEM model of the utilized plate with indicators for excitation (x) and a dashpot damper (o).

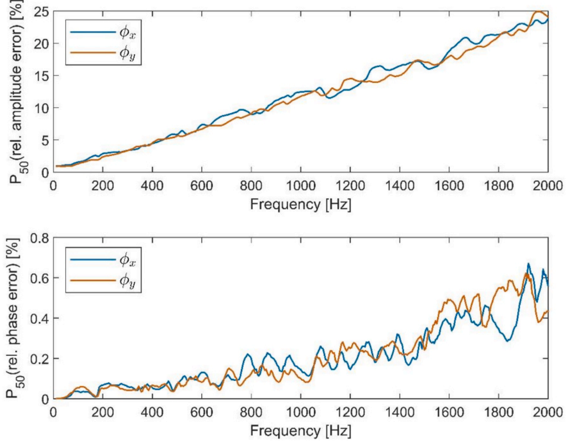

Fig. 4.3. Median of the relative error of complex nodal rotation values (magnitude and phase) between the reference and reduced datasets about the x- and y-axes, top: magnitude, bottom: phase.

the approximation has nearly no impact on the phase.

The error emerges because the approximation is performed only on the basis of the nodal displacement. This means that the approximated rotations represent only the geometric rotations that match the current displacement field. However, in the FEM, the nodal rotations of shell elements are used as degrees of freedom during the simulation. Therefore, the resulting rotations from the FEM simulation not only represent the rotations of the current displacement field but also include shear- and bending-related rotations. In the case of this work, only bending-related rotations, such as the Kirchhoff plate theory, are applied.

The linear trend of the rotation approximation error is only linear in the investigated frequency range considered in this work. The actual trend of the approximation error rather follows a root-function. The reason for this is the constant mesh density that is used over the investigated frequency range. The wavelength decreases over frequency, and the fewer elements are available per wavelength λ, the larger the error of the rotation approximation ε_φ. In other words, the error is inversely proportional to the wavelength $\varepsilon_\varphi \propto \frac{1}{\lambda}$, with the wavelength being proportional to the inverse of the root of the angular velocity $\lambda \propto \frac{1}{\sqrt{2\pi f}}$. This means that the error of the rotation approximation is described by $\varepsilon_\varphi \propto \sqrt{2\pi f}$, but in the investigated frequency range, the root function trend is not yet recognizable.

This also implies that the accuracy of the approximation is sensitive to the mesh resolution. Considering the same setup of the numerical model but using different mesh densities, this effect becomes apparent. In Fig. 4.4, the rotation approximation error over frequency is shown for three mesh densities. The mesh density 'm' represents the density specified earlier in this chapter. The densities '2m' and 'm/2' represent the approximation errors for meshes with twice and half the number of elements in both room directions, respectively. The trends of the approximation errors for the three mesh densities show that a doubling of the elements in both room directions results in an error reduction of a factor of four. Conversely, the error increases by a factor of four when the number of

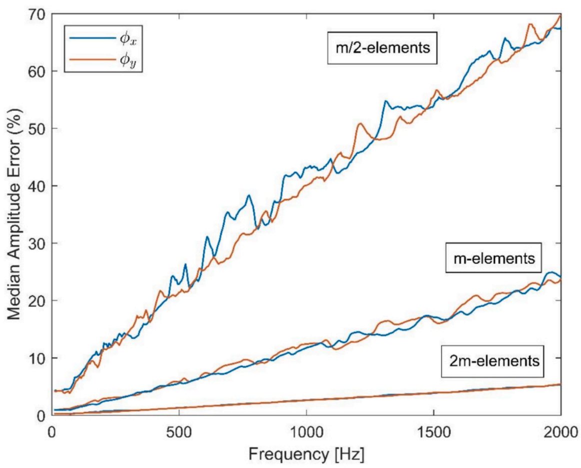

Fig. 4.4. Influence of the element density on the nodal rotation approximation error between the reference and reduced datasets.

elements per room direction is reduced by a factor of two. Also, in case of the mesh density 'm/2', the root function trend, described in the previous paragraph, becomes recognizable. The error curve shows a decreasing slope above roughly 1000 Hz compared to the region below 1000 Hz.

At this point, an error, which is introduced during the calculation of the nodal rotations, needs to be addressed. That is, the averaging of the elemental rotations on adjacent nodes (see Eq. (3.5) as a reference). The rotations in the reference dataset exist only on the nodes and are a result of the FE simulation. In the case of the reduced dataset, the rotations are calculated in the element's centroid, and only after that, the averaging takes place to acquire approximated nodal rotations. Therefore, a direct comparison to quantify the impact of averaging is not possible. Accordingly, the following approach has been chosen to investigate the averaging error. The shape function approach (see Eq. (8.22) through Eq. (8.25) in the Appendix as a reference) $\varphi_{\mathrm{element}} = \sum_{\mathrm{i}=1}^{4} \mathrm{N_i} \bullet \varphi_{\mathrm{node,i}}$ is utilized to calculate the elemental rotations for the reference dataset. While this might also introduce an error, it is assumed that this error is significantly smaller than the error introduced by the averaging procedure in the reduced dataset. By comparing the two elemental rotation datasets, the error that results from the elemental rotation approximation in the reduced dataset is acquired; see Fig. 4.5. A maximum error of approximately 10% at 1980 Hz is introduced during the approximation. Considering the results of the total rotation approximation error from Fig. 4.3 at 1980 Hz, the averaging procedure to acquire the nodal rotations in the reduced dataset is responsible for the remaining error increase of approximately 15%. Even though averaging introduces an error, it is a pragmatic approach that allows efficient acquisition of nodal rotations while considering regular grids. In the case of irregular grids, averaging might have a much greater impact. A detailed evaluation of this error and an alternative approach to acquire nodal rotations from the elemental rotations for irregular grids lies beyond the scope of this work.

Another impact on the rotation approximation needs to be addressed, i.e., discontinuities in the structure. In the case of this work, discontinuities exist along the boundary conditions of the plate only, i.e., the clamped edges. The rotation approximation uses the translatory response of the nodes. Nodes that are part of the boundaries do not experience a translatory response. However, elemental rotations about both axes, i.e., the x-axis and y-axis, are calculated according to Eq. (3.2) and Eq. (3.3), respectively. A rotation acting perpendicular to an edge, which is calculated by using the boundary nodes, results in a value that is not physically accurate. The reason is that the rotation that results is only based on the translatory response of the two nodes, which are not part of the boundary. Therefore, either no rotation or torsion of the element can result, depending on the phase relation between the two nonbounded nodes. This subsequently affects the resulting STI vector near the boundaries. Special care should be taken when evaluating STI results in the vicinity of discontinuities. The first line of elements along discontinuities is especially prone to this error. A possible way to handle this error close to discontinuities is to increase the local mesh density.

4.2. Calculation of the elemental force and moment data

The relative errors for the magnitudes of the elemental forces and moments over frequency are presented in Fig. 4.6. The errors for the normal forces are not displayed, as they are zero (exactly zero, considering a rounding of the resulting percent values to two decimals) and therefore neglected. The normal forces are calculated precisely. The moments are computed via the approximated nodal rotations. The relative errors of the moment magnitudes are approximately 24% at their maximum. The reason for this error is that during the calculation of the moments, the rotational nodal data are used directly and therefore propagate the error into the elemental moment values.

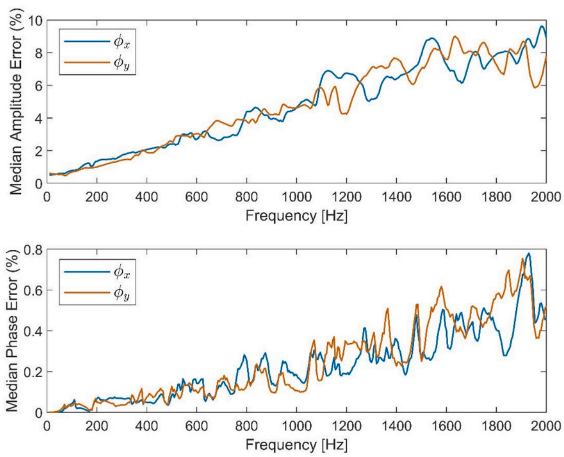

Fig. 4.5. Median relative error of complex elemental rotation values (magnitude and phase) between the reference and reduced datasets about the x- and y-axes; top: magnitude; bottom: phase.

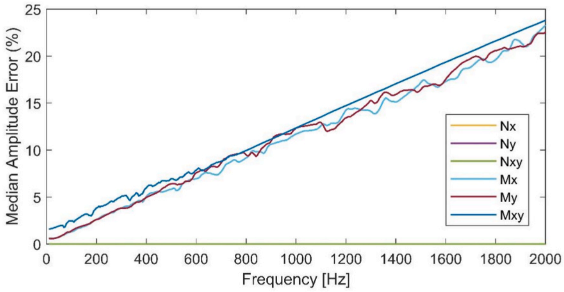

Fig. 4.6. Median of the relative magnitude error of the elemental forces (N_x, N_y, N_{xy}) and moments (M_x, M_y, M_{xy}) over frequency between the reference and reduced datasets.

4.3. *Error in resulting structural intensity vector fields*

The STI vectors are calculated via Eq. (2.5) for every element. The resulting STI vector fields combine the translatory and rotational nodal values and the elemental rotation, force and moment values. Errors in the forces and moments are propagated to the resulting STI vector fields. Therefore, it is necessary to quantify these errors. This subsection presents an approach to compare vector fields in terms of their similarity in magnitude and phase. The reference ('ref') and reduced ('red') datasets are subsequently compared to quantify the errors in magnitude and phase.

The relative magnitude error of a vector field over the whole geometry at a specific frequency is calculated by

$$\xi_{rel}(f) = \left| \left| \overrightarrow{I}_{red}(f) \right| - \left| \overrightarrow{I}_{ref}(f) \right| \right| \oslash \left| \overrightarrow{I}_{ref}(f) \right| \tag{4.2}$$

where $\overrightarrow{I}$ is a matrix of dimension (n x 3), where n describes the number of individual vectors and the second entry is the number of spatial dimensions (x, y, z). The $\oslash$-operator describes the Hadamard division [37], an elementwise division of vectors or matrices with the same dimensions. The relative error of the overall vector field direction is calculated on the basis of the cosine similarity while calculating the actual angle difference and referencing it to π with

$$\forall \left(n \in \overrightarrow{I} \right) : \psi_{rel,f}(n) = \frac{1}{\pi} \cos^{-1} \left[\left(\frac{\overrightarrow{I}_{ref,f}(n)}{\left| \overrightarrow{I}_{ref,f}(n) \right|} \right) \bullet \left(\frac{\overrightarrow{I}_{red,f}(n)}{\left| \overrightarrow{I}_{red,f}(n) \right|} \right) \right] \tag{4.3}$$

The vector matrices are normalized, and the dot-product (•) is calculated for every vector pair. Taking the arc cosine of the product gives the absolute angle difference between vector pairs in radians. By dividing by π, a relative error is obtained. The error ranges between zero and one, with one describing a phase difference between the vectors of π or 180° when considered in degrees.

The median relative errors of the magnitude and phase of the STI vector fields over frequency are presented in Fig. 4.7. The relative error of the magnitude is approximately 19% at its maximum and shows a similar linear trend as the nodal rotation error in Fig. 4.3 in this investigated frequency range. The phase error does not exceed 1% at its maximum and shows a linear upward trend as well; however, the slope is significantly smaller than the magnitude.

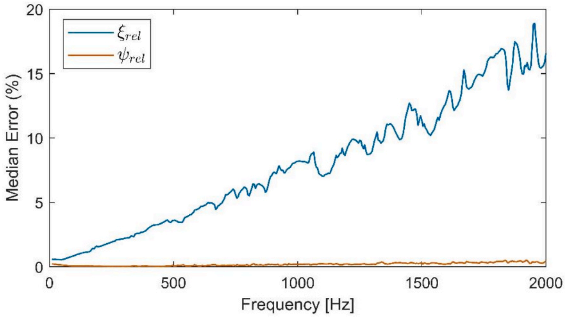

Fig. 4.7. Median of the relative error for vector-pair magnitudes and angle deviation per frequency line of the STI vector fields calculated with the plate FE model.

5. Validation of the hybrid method with experimental results

Experiments are conducted to validate the proposed method and to demonstrate how well the hybrid method performs on experimental data, as well as the accuracy of the comparison between the numerical and experimental results. For validation, a set of STI vector fields calculated from experimental data is compared with a vector field obtained from numerical results generated with an FE model. The hybrid method is used to obtain the STI vector fields from the experimental data. Consistent with the previous evaluation of the numerical data, the Kirchhoff plate theory is applied to evaluate the forces and moments at the element centroids. For the numerical data, the full set of FEM results is used, providing all necessary information to calculate the STI vectors according to Eq. (2.5).

Fig. 5.1 shows the CAD geometry of the laboratory structure used in the experiment. However, the FEM model only consists of an inner bending panel with a size of 450 mm × 300 mm. The frame is idealized as a clamped support for the inner bending panel. The laboratory structure has been manufactured from a tempered monolithic aluminum block by milling to create a clamped plate-like bending panel with a minimum residual stress. Owing to the accurate milling process, the resulting bending panel only contains minimal uncertainties along its edges regarding the stiffness between the plate section and the frame because of the fillet radius from the milling tool. The backside of the plate is the original surface of the aluminum block and is flat over the entire structure. The laboratory structure is characterized by a Young's modulus of E=70 GPa, a density of ρ=2660 kg/m^3, and a Poisson's ratio of ν=0.34.

The following setup aims to provide an easy-to-set measurement capable of creating a reproducible source–sink characteristic in a structure that leads to STI vector fields showing distinctive paths. The reason for using a source–sink characteristic in the structure for this paper has been explained while setting up this FE model of the plate structure in Section 4. In short, more distinctive STI vector fields should be produced when a setup with a discrete source and sink is used than when material damping alone is considered the dissipative mechanism. Furthermore, the acquired measurement data allow the testing of dedicated path identification techniques on experimental data in future studies.

The plate structure is excited via two electrodynamic shakers (TIRA 51120-MOSP) attached perpendicular to the surface, as shown in Fig. 5.2, which utilize appropriate stingers to prevent excitation via moments. A glue connection has been used for attachment to the plate. The excitation is performed with two signals, of which the second has a 180-degree phase shift. Both shakers use the same excitation signal as a pseudorandom signal with band limits of 10–2000 Hz at a sample rate of 12.8 kHz. At both attachment locations, impedance heads (PCB – ICP model 288D01) are used to measure the acceleration and force response simultaneously. Both shakers are set up to excite the structure with a similar magnitude. During a test measurement, the root-mean square of the force signal time-series determines the magnitude of the setup's excitation force.

The idea behind this setup is to create a discrete number of states in the system at which the phase of *Shaker 2* (upper left shaker in Fig. 5.2) and the phase of the plate's response, at the shaker attachment location, are ideally shifted by 90°. This concept would mean that this position on the plate is attenuated and should act as a local dissipation sink. Therefore, paths between the source, with *Shaker 1* (the lower right shaker in Fig. 5.2) and *Shaker 2,* should emerge in the resulting STI vector fields. This claim is an open question as to whether only an exact shift of 90° results in sufficient attenuation of the plate or if deviations from this ideal phase shift are sufficient. The reason that attenuation over the full frequency range is not possible with this setup is as follows. Both shakers are driven with a pregenerated signal that is not altered throughout the excitation. The plate acts as a transfer element between the shaker attachment locations. Before the measurement, it is impossible to estimate the plate response behavior exactly; therefore, it is impossible to design a driving signal for the shaker that allows attenuation of the plate at a certain point over a wide frequency range.

Alternative approaches to acquire a state of attenuation over a wide frequency range would require dissipating components such as a viscous damper or a controlled feedback loop. A dissipative component in the form of a viscous damper has its own frequency-

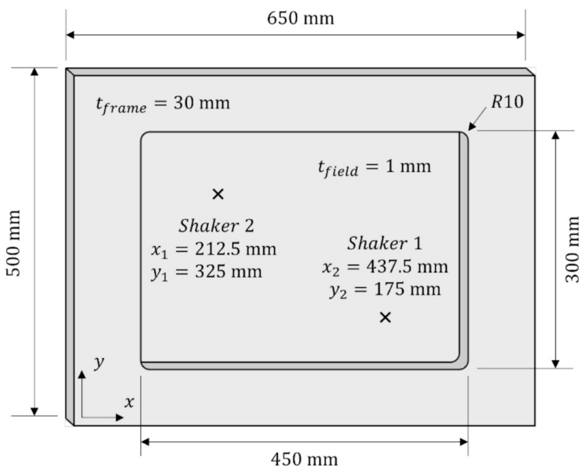

Fig. 5.1. Laboratory plate structure overview.

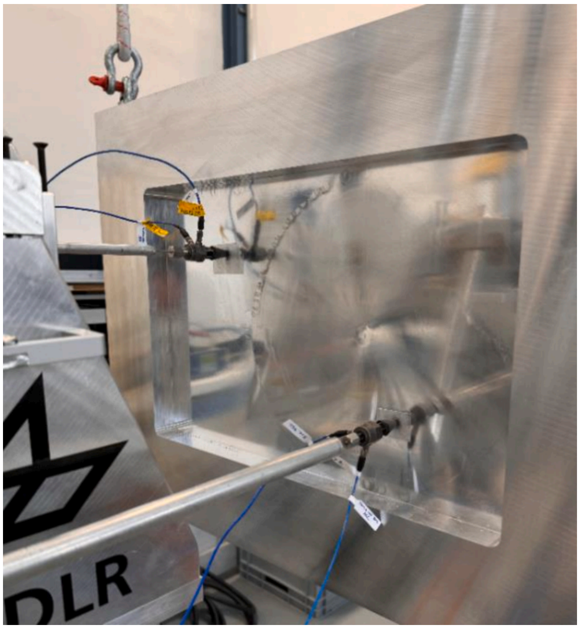

Fig. 5.2. Experimental two-shaker setup (left) and attachment connector (right).

dependent behavior, and including its behavior in an FE model is not trivial. A controlled feedback loop controls the driving signal of *Shaker 2* via a second stationary LDV scanning point near the attachment location of the shaker. By tuning the control loop to minimize the plate's response, one acquires attenuation over a specific frequency range. However, this approach requires additional equipment and is time-consuming and cost-intensive. Therefore, the chosen two-shaker setup is preferable because of its simplicity and ability to be easily rebuilt in the laboratory. Even though only a discrete number of frequency lines will result in sufficient attenuation, these data will help validate the theory and test new developments in the future.

The structural response of the plate is measured via an LDV. The flat backside of the plate acts as the measurement surface and is prepared with a retroreflective spray to ensure a sufficient signal-to-noise ratio of the laser beam. A total of 925 points are measured in the area of the bending panel of the plate. An acquisition time of 15 s per point and a sample rate of 12.8 kHz have been used. The measurement grid contains only 37 points along the x-axis and 25 points along the y-axis on the inner bending panel. All the points are equally spaced, resulting in a geometric resolution of 12.5 mm between the measurement points. The mesh matches the mesh of the numerical model, described in Section 4, exactly. Accordingly, the mesh can capture the plate's structural response up to 2000 Hz. Model updating has been performed to match the structural response of the FEM qualitatively to the structural response acquired during an experiment that is later covered in Section 5. The updating has been performed via the frequency-domain assurance criterion (FDAC) [38] as the basis for the objective function, and a gradient-based optimization method [39] has been used to adapt the optimization parameters (Young's modulus and density) iteratively. The material parameters used follow the values stated in Section 4.

The time-series data that has been acquired with the LDV is transformed into the frequency-domain via discrete Fourier

Table 5.1
Frequencies of matching STI vector fields for the experimental and numerical datasets with deviations in reference to the numerical dataset.

FEM	Measurement	Deviation
85 Hz	85 Hz	0%
265 Hz	265 Hz	0%
330 Hz	330 Hz	0%
420 Hz	440 Hz	5%
670 Hz	690 Hz	3%
750 Hz	770 Hz	3%
875 Hz	890 Hz	2%
950 Hz	965 Hz	2%
1040 Hz	1065 Hz	2%
1330 Hz	1360 Hz	2%
1710 Hz	1745 Hz	2%
1875 Hz	1930 Hz	3%

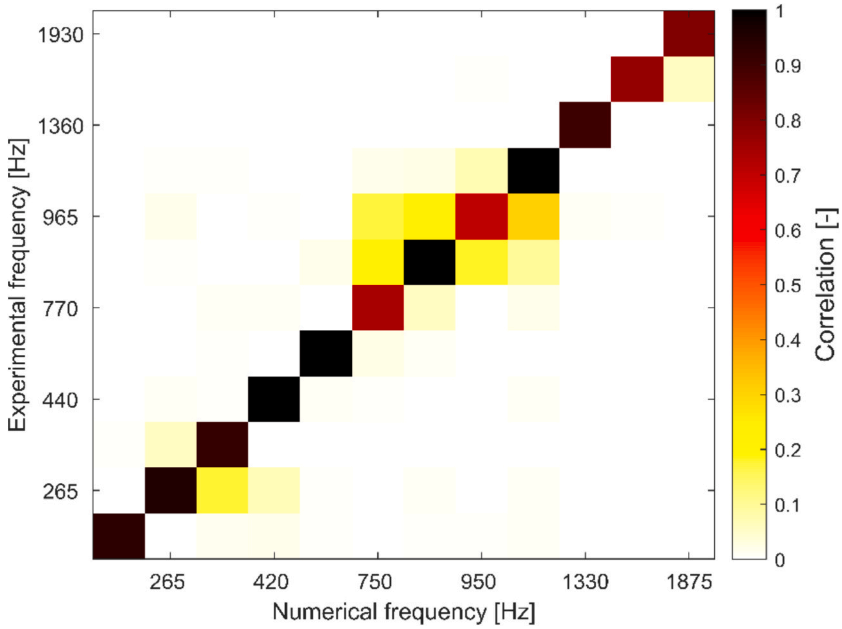

Fig. 5.3. FDAC evaluation between the experimental and numerical datasets at discrete frequencies that show distinct path characteristics in the STI vector fields.

transformation. For the estimation of frequency response functions (FRFs), Welch's method [40] is used, utilizing the H1 estimator with the response spectra referenced to the force spectrum of the impedance head of *Shaker 1*. The H1 estimator is selected because it is assumed that the noise in the response signal is more significant. A Hanning window with an overlap factor of 0.66 is used as a window function.

5.1. Comparison of experimental and numerical datasets

During the evaluation of the measurement data, 12 discrete frequencies have been identified that show STI vector fields with distinct path characteristics. The frequencies have been identified by visually comparing the STI vector fields from the experimental and numerical datasets in a similar frequency range. The discrete frequencies are spaced out over the full considered frequency range of 10–2000 Hz; see Table 5.1. Even though the FE model has been updated, small deviations in frequency persist. The deviations in the frequencies show that, compared with the laboratory plate structure, the FE model slightly underestimates the frequency response of the plate.

A correlation of the structural response datasets has been performed via FDAC. FDAC uses the FRFs of two datasets to calculate a normalized scalar product over all considered frequencies. In this work, only the scalar products of the frequency pairs shown in Table 5.1 are calculated; see Fig. 5.3. This analysis allows an investigation of how well the respective plate responses of the experimental and numerical datasets are correlated. The plot indicates a high correlation between the structural response of the experimental structure and the numerical model. The lowest correlation value is 0.7 at the frequency pair 950 Hz/965 Hz.

Additionally, the previously discussed phase shifts between the force signal of the impedance head at the attachment location of

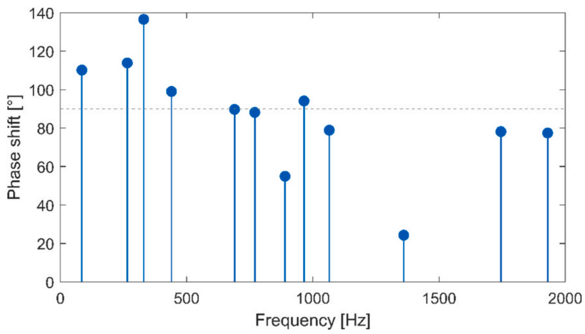

Fig. 5.4. Phase shift between the reference signal and structural response at the location of shaker 2 for the experimental setup.

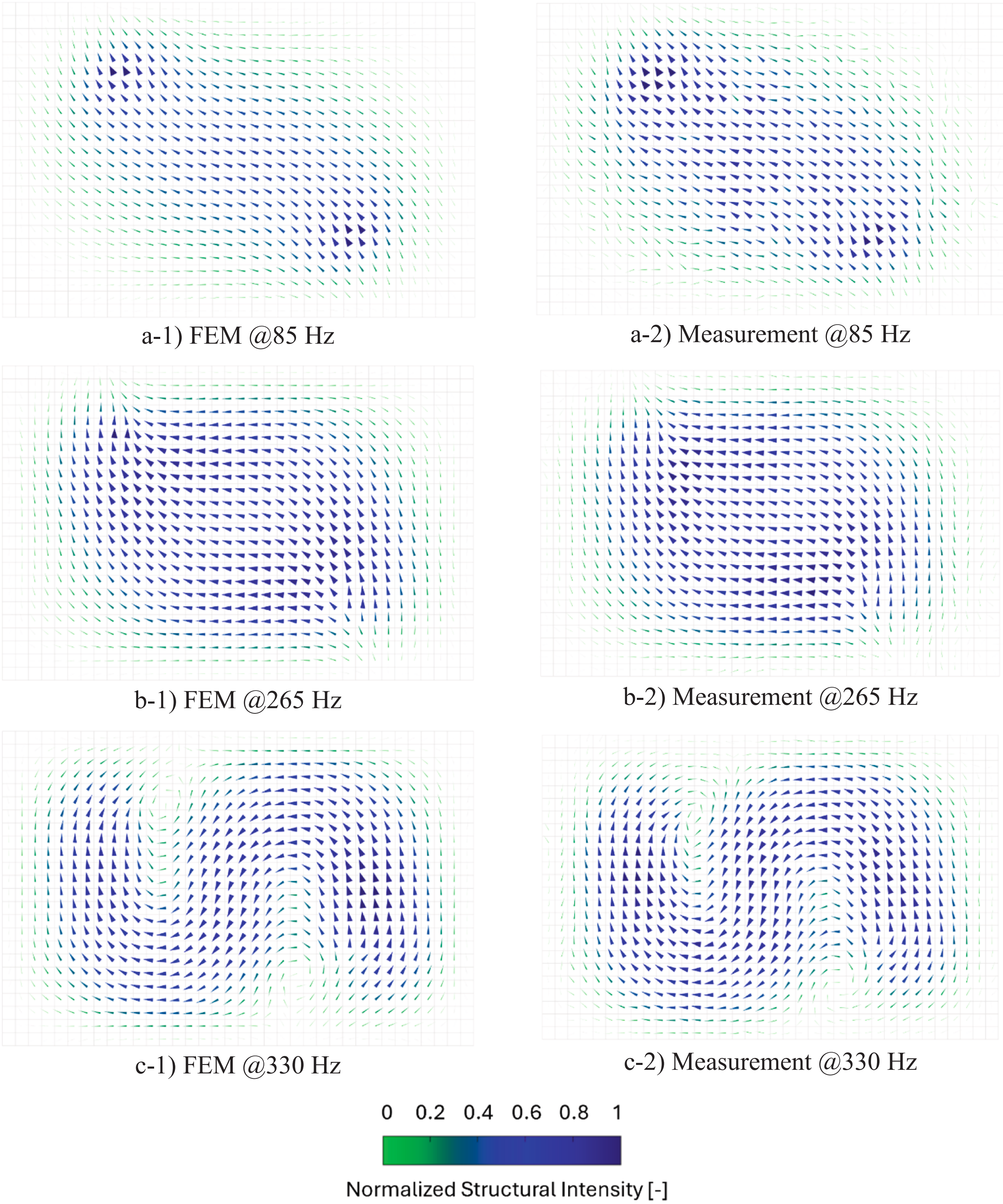

Fig. 5.5. Normalized STI – numerical (left) and measurement (right) at 85 Hz, 265 Hz, and 330 Hz.

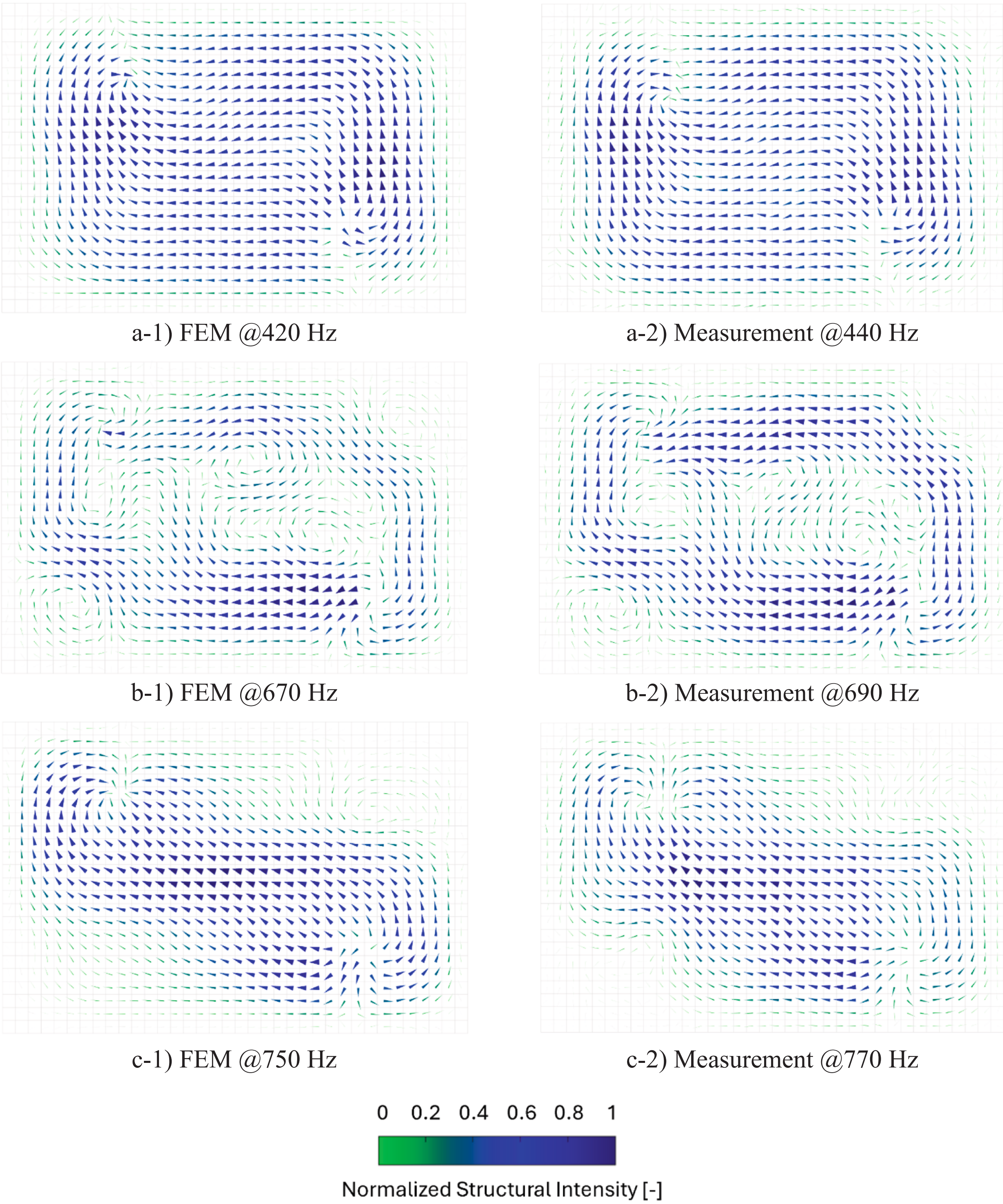

Fig. 5.6. Normalized STI – numerical (left) and measurement (right) at the frequency pairs of 420/440 Hz, 670/690 Hz, and 750/770 Hz.

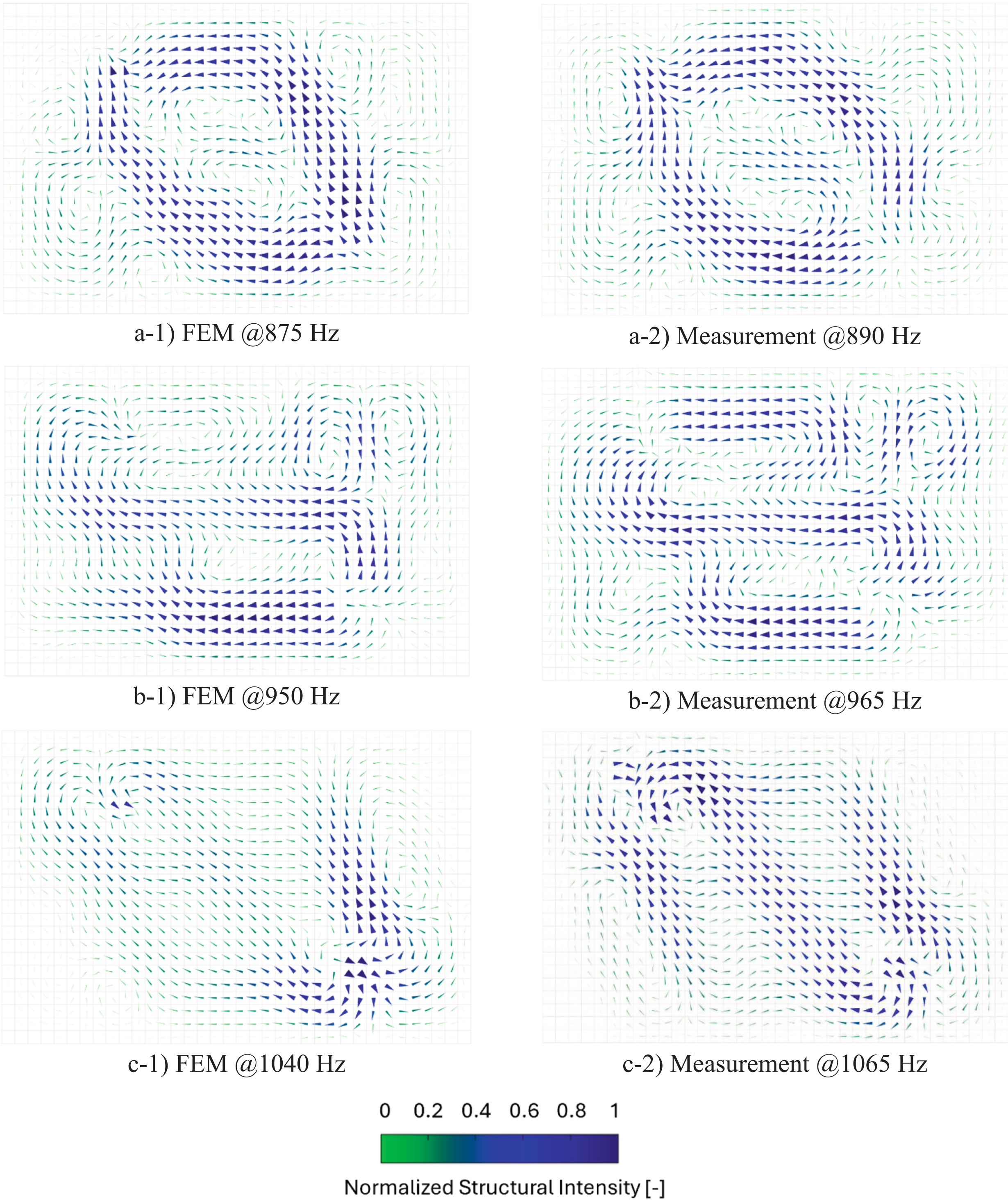

Fig. 5.7. Normalized STI – numerical (left) and measurement (right) at the frequency pairs 875/890 Hz, 950/965 Hz, and 1040/1065 Hz.

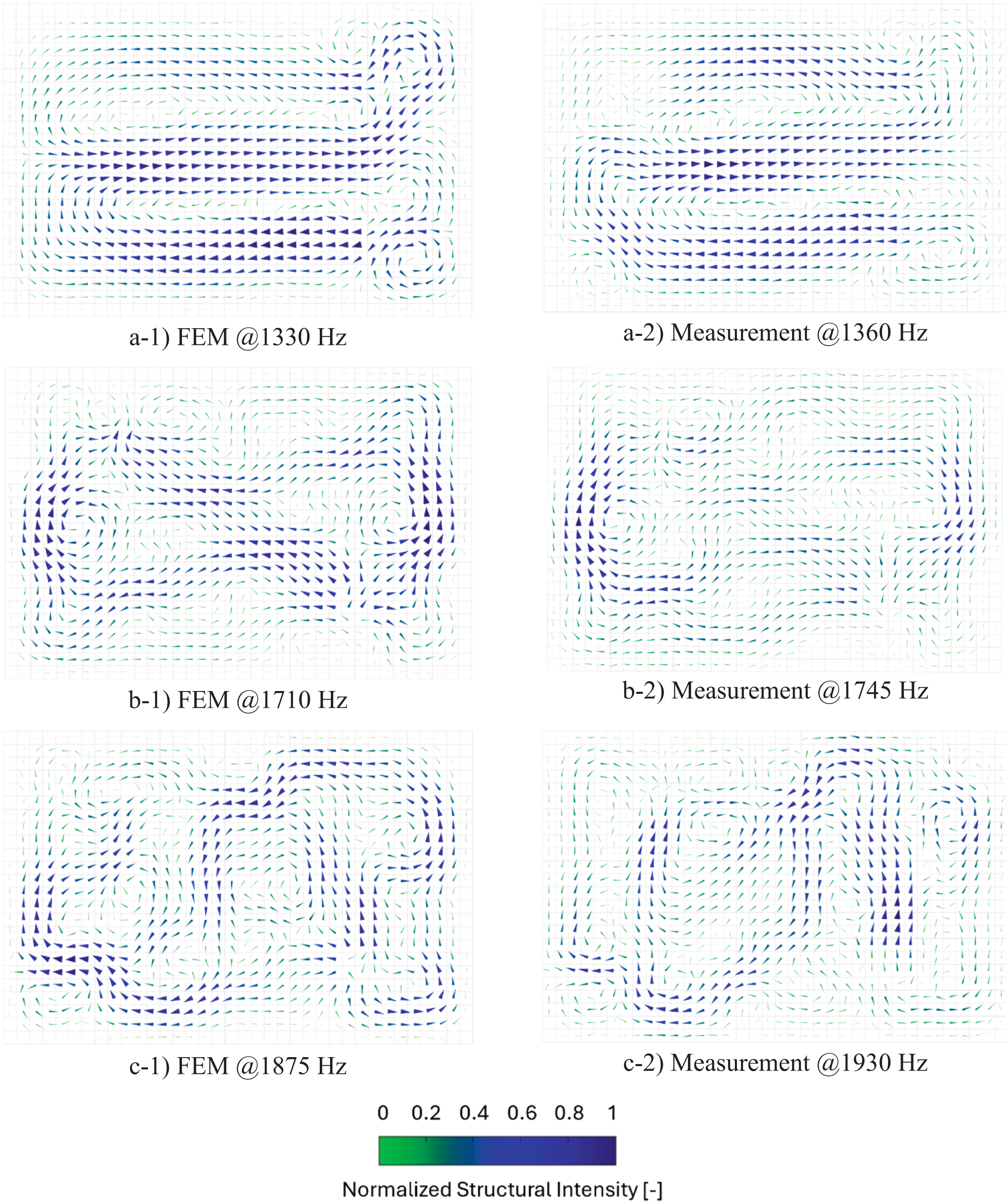

Fig. 5.8. Normalized STI – numerical (left) and measurement (right) at the frequency pairs 1330/1360 Hz, 1710/1745 Hz, and 1875/1930 Hz.

Shaker 2 and the plate response at the respective location are investigated. In Fig. 5.4, the phase shifts for the frequencies in the 'Measurement' column of Table 5.1 are presented. The phase shift is close to 90° only for the 670 Hz, 750 Hz, and 950 Hz frequencies. For all other frequencies except at 330 Hz, 875 Hz, and 1330 Hz, the phase shift ranges from ±30° to the desired 90° phase shift. Even though the phase shift is not close to 90° for all identified frequencies, the following STI vector field comparison shows that source–sink pairs exist in the structural response of the structure. Therefore, creating a perfect 90° phase shift is unnecessary to acquire a source–sink characteristic to create distinct paths in a structure.

The STI vector fields for the first set of frequencies are presented in Fig. 5.5. The vector magnitudes are normalized to the largest STI amplitude at the respective frequency. Cones are used to visualize the vectors. The width of the cones correlates with the color map. This results in cones with a thinner base for low STI magnitudes and allows the observer to focus on the significant parts of the vector field. The excitation location in the lower right corner is clearly visible in the numerical data. The vector fields at these relatively low frequencies show simple paths due to the large wavelengths and the corresponding plate response with global characteristics. The power flows take a more or less direct path to the sink in the upper left corner except for the STI vector field at 330 Hz, which flows in a double curved path in the form of a letter 'S' lying on its side. The corresponding vector fields of the experimental dataset exhibit very similar, almost identical, behavior.

The paths in the STI vector fields at 420 Hz, 670 Hz, and 750 Hz (referencing the frequencies of the numerical dataset) become more complex because of the decreasing wavelengths (see Fig. 5.6). Additionally, for this set of frequencies, the experimental and numerical data show high similarity between the fields. Even small details, such as curls, are represented in the measurement data. Additionally, the visual comparison shows a good match between the experimental and numerical data for the following sets of discrete frequencies in Fig. 5.7 and Fig. 5.8. The evaluated frequencies provide a concise picture of the applicability of the proposed hybrid method over the full frequency range of the acquired measurement data.

6. Conclusion

This work aims to provide an exhaustive description and detailed quantification of the accuracy of the so-called hybrid method, which allows the approximation of structural intensity (STI) vector fields from the measured vibration response of thin-walled structures. The goal is to provide a comprehensive analysis of the hybrid method's performance to allow researchers and engineers in various fields to use this work in their evaluations or as a basis to adopt it for their work.

A verification via two artificial datasets from a finite element model is performed. One of the datasets holds all the necessary information to calculate the STI vectors directly, whereas the second dataset contains only the translational nodal response data. Nodal rotation and the elemental forces and moments require approximation for the second dataset. The verification of these datasets reveals that STI vector fields are approximated with high accuracy in terms of qualitative aspects, i.e., flow characteristics. The median angle deviation of the vector fields of both datasets results in values below 1%. The deviations in the magnitudes are more significant. The magnitude error shows a linear dependency over the investigated frequency range and results in a maximum error of 19%. The reason for this error is the approximation of the nodal rotations. The error of the nodal rotations also shows a linear dependency over the investigated frequency range, with a maximum of 25%. The error during the nodal rotation approximation occurs because only the geometric deflections of the structural response are used to approximate the rotation values. However, the nodal rotations in finite element (FE) simulations are an additional degree of freedom. Therefore, the nodal rotation values not only represent the respective structural response of the plate but also include rotation information concerning the bending moment and its respective energy equilibrium calculated during the FE simulation. Furthermore, the averaging procedure to acquire the nodal rotations on the basis of the approximated elemental rotations introduces an additional significant error. However, this error is already considered in the total rotation approximation error stated previously in this paragraph. This opens the possibility of improving the hybrid method in the future. A significant error reduction could be achieved by improving or bypassing the averaging procedure.

During the verification, the correlation between the nodal rotation error and the mesh density has been evaluated. The results indicate that the approximation error decreases with increasing mesh density and vice versa. In terms of the observed characteristics of the magnitude and phase errors during the verification of this work, the phase errors are two orders of magnitude lower than the magnitude errors. However, a general statement remains impossible since only one structure has been investigated in this paper. Additionally, special care is required when evaluating the STI near discontinuities, such as boundaries. The rotation approximation introduces erroneous rotations in the first row of elements adjacent to these discontinuities. This occurs because the rotation is computed from a set of nodes, some of which lack translational response because they are located on the discontinuity.

For the validation, an experimental setup, in the form of a two-shaker excitation acting on a plate structure, has been used. This setup creates structural responses in the plate, leading to STI fields showing distinct path characteristics at twelve discrete frequencies. The STI vector fields are validated against an FE model using the measurement data. The validation has been successful with respect to the qualitative aspects of the vector fields. For all twelve frequencies, the vector fields present almost exact flow characteristics.

In conclusion, the verification and validation results indicate that the hybrid method provides accurate results regarding the qualitative approximation of STI vector fields. The magnitudes of the vectors depend on the available information regarding the damping factors and the applicable mesh density. The experimental setup performs well in terms of the generation of distinct path characteristics in STI vector fields. This approach helps to perform repeatable measurements without a complex setup. This conclusion is especially true with the respective FE model described in this paper. This method can be used to validate the hybrid method, allowing for the testing of dedicated path identification approaches in the future.

Although referring to plate elements in this work, shell elements with the appropriate degrees of freedom have been used, meaning that the acting loads in curved structures are still represented within the formulation. Therefore, this method is also suitable for large-scale structures with curvatures, such as aircraft components, i.e., fuselages, wings, and automotive structures, as long as thin-walled structures are investigated. First numerical tests of the hybrid method applied to a curved structure, i.e., a simple cylinder shell model, have indicated promising results. Accordingly, users are advised to proceed with caution, given that no definitive performance bounds for the hybrid method on curved structures can currently be stated. For now, the hybrid method is recommended only for meshes whose discretization yields elements that can reasonably be assumed to behave in a plate-like manner. An application to structures featuring strongly warped elements might require other elements with higher-order shape functions or a finer mesh discretization with 4-node-elements and linear shape functions.

CRediT authorship contribution statement

Sebastian F. Zettel: Conceptualization, Methodology, Investigation, Validation, Visualization, Writing – original draft, Writing – review & editing. **René Winter:** Conceptualization, Writing – review & editing, Supervision. **Marc Böswald:** Writing – review & editing, Supervision, Conceptualization. **Marcus Maeder:** Writing – review & editing, Supervision. **Steffen Marburg:** Writing – review & editing, Supervision.

Declaration of competing interest

The authors declare that they have no known competing financial interests or personal relationships that could have appeared to influence the work reported in this paper.

Appendix

6.1. Calculation of element forces and moments

The fundamental concept of the FEM is the description of continuous displacements inside an element by using the nodal displacements and a set of shape functions. This section describes the equations necessary to calculate the forces and bending moments in the elements by using bilinear shape functions for quadrilateral four-node plate elements. The kinematics are defined by the Mindlin–Reissner plate theory [27]

$$\underline{u}_x(z) = \underline{u}_x + z\,\underline{\varphi}_y \tag{8.1}$$

$$\underline{u}_y(z) = \underline{u}_y - z\,\underline{\varphi}_x \tag{8.2}$$

$$\underline{u}_z(z) = \text{const.} \tag{8.3}$$

with the complex displacement $\underline{u}$ and complex rotations $\underline{\varphi}$ in the frequency-domain (see Eq. (2.3) as a reference) according to the global coordinate system (x, y, z). The z-axis in the shell-thickness direction originates in the mid-plane of the plate. In relation to the STI calculation presented in Eq. (2.5) and considering the plate theory in Eq. 8.1–8.3, the missing forces and moments are calculated by [41]

$$\underline{N}_x = \frac{Eh}{1-\nu^2}\left(\underline{\epsilon}_{x,l} + \nu\underline{\epsilon}_{y,l}\right) \tag{8.4}$$

$$\underline{N}_y = \frac{Eh}{1-\nu^2}\left(\underline{\epsilon}_{y,l} + \nu\underline{\epsilon}_{x,l}\right) \tag{8.5}$$

$$\underline{N}_{xy} = \frac{Eh}{1-\nu^2}\,\frac{1-\nu}{2}\,\underline{\epsilon}_{xy,l} \tag{8.6}$$

$$\underline{Q}_{xz} = \frac{\kappa_{12,xz}\,Eh}{2(1+\nu)}\,\underline{\epsilon}_{xz} \tag{8.7}$$

$$\underline{Q}_{yz} = \frac{\kappa_{12,yz}\,Eh}{2(1+\nu)}\,\underline{\epsilon}_{yz} \tag{8.8}$$

$$\underline{M}_x = \frac{Eh^3}{12\,(1-\nu^2)}\left(\underline{\epsilon}_{x,b} + \nu\underline{\epsilon}_{y,b}\right) \tag{8.9}$$

$$\underline{M}_y = \frac{Eh^3}{12\,(1-\nu^2)}\left(\underline{\epsilon}_{y,b} + \nu\underline{\epsilon}_{x,b}\right) \tag{8.10}$$

$$\underline{M}_{xy} = \frac{Eh^3(1+\nu)}{12(1-\nu^2)}\underline{\epsilon}_{xy,b} \tag{8.11}$$

where $\underline{N}_i$ describes the complex normal force, $\underline{Q}_i$ represents the complex transverse shear forces, $\underline{M}_i$ represents the complex moments, $\underline{\epsilon}_i$ represents the complex strains, all in the frequency-domain, and κ_1 represents the through-thickness correction factor according to Timoshenko et al. [15]. The subscripts l and b indicate longitudinal and bending strains, respectively. The material properties are described by E the Young's modulus, the shell thickness h, and Poisson's ratio ν. In Fig. 8.1, the internal forces and moments for a plate element are shown.

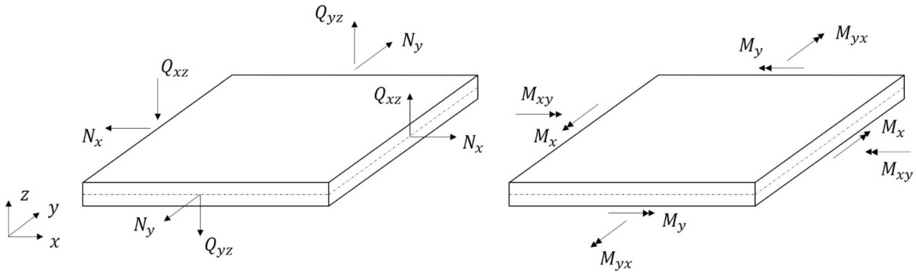

Fig. 8.1. Plate element internal forces

The calculations of element forces and moments are performed on the mid-planes of the elements. However, measurements of vibrating structures are performed on the surface and not in the respective mid-plane of the structure. According to the in-plane plate kinematics described in Eq. (81) and Eq. (82), one acquires the true mid-plane deformations by transforming the deformations measured on the surface to the mid-plane. This transformation is performed by using $\underline{u}_x = \underline{u}_x(z) - z\underline{\varphi}_y$ and $\underline{u}_y = \underline{u}_y(z) + z\underline{\varphi}_x$ for deformations in the x- and y-directions, respectively. Considering the missing rotational DOFs at the nodes of the acquired measurement data, the transformation above is only possible after the respective approximation of the nodal rotations described in Section 3.

In relation to the chosen Mindlin plate theory, one calculates the respective strains in Eq. (8.4) to Eq. (8.11) by [42]

$$\epsilon_{x,l} = \frac{\partial u_x}{\partial x} \tag{8.12}$$

$$\epsilon_{y,l} = \frac{\partial u_y}{\partial x} \tag{8.13}$$

$$\epsilon_{xy,l} = \frac{\partial u_x}{\partial y} + \frac{\partial u_y}{\partial x} \tag{8.14}$$

$$\epsilon_{x,b} = -\frac{\partial \varphi_y}{\partial x} \tag{8.15}$$

$$\epsilon_{y,b} = -\frac{\partial \varphi_x}{\partial y} \tag{8.16}$$

$$\epsilon_{xy,b} = \frac{\partial \varphi_x}{\partial y} - \frac{\partial \varphi_y}{\partial x} \tag{8.17}$$

$$\epsilon_{xz} = \frac{\partial u_z}{\partial x} + \varphi_y \tag{8.18}$$

$$\epsilon_{yz} = \frac{\partial u_z}{\partial y} - \varphi_x \tag{8.19}$$

In the FE context, one rewrittes the partial differentials in Eq. 8–12 to Eq. 8–19 by using shape functions N_i for every node of an element and their partial differentials $\partial N_i/dx$ and $\partial N_i/dy$ by

$$\begin{Bmatrix} \underline{\epsilon}_{x,1} \\ \underline{\epsilon}_{y,1} \\ \underline{\epsilon}_{xy,1} \end{Bmatrix} = \begin{bmatrix} \frac{\partial N_1}{dx} & 0 & \cdots & \frac{\partial N_4}{dx} & 0 \\ 0 & \frac{\partial N_1}{dy} & \cdots & 0 & \frac{\partial N_4}{dy} \\ \frac{\partial N_1}{dx} & \frac{\partial N_1}{dy} & \cdots & \frac{\partial N_4}{dx} & \frac{\partial N_4}{dy} \end{bmatrix} \begin{Bmatrix} \underline{u}_{z,1} \\ \underline{u}_{y,1} \\ \vdots \\ \underline{u}_{z,4} \\ \underline{u}_{y,4} \end{Bmatrix} \tag{8.20}$$

$$\begin{Bmatrix} \underline{\epsilon}_{x,b} \\ \underline{\epsilon}_{y,b} \\ \underline{\epsilon}_{xy,b} \\ \underline{\epsilon}_{xz} \\ \underline{\epsilon}_{yz} \end{Bmatrix} = \begin{bmatrix} 0 & 0 & -\frac{\partial N_1}{dx} & \cdots & 0 & 0 & -\frac{\partial N_4}{dx} \\ 0 & \frac{\partial N_1}{dy} & 0 & \cdots & 0 & \frac{\partial N_4}{dy} & 0 \\ 0 & \frac{\partial N_1}{dy} & -\frac{\partial N_1}{dx} & \cdots & 0 & \frac{\partial N_4}{dy} & -\frac{\partial N_4}{dx} \\ \frac{\partial N_1}{dx} & 0 & N_1 & \cdots & \frac{\partial N_4}{dx} & 0 & N_4 \\ \frac{\partial N_1}{dy} & -N_1 & 0 & \cdots & \frac{\partial N_4}{dy} & -N_4 & 0 \end{bmatrix} \begin{Bmatrix} \underline{u}_{z,1} \\ \underline{\varphi}_{x,1} \\ \underline{\varphi}_{y,1} \\ \vdots \\ \underline{u}_{z,4} \\ \underline{\varphi}_{x,4} \\ \underline{\varphi}_{y,4} \end{Bmatrix} \tag{8.21}$$

considering four node shell elements [41]. The matrices containing the partial differentials of the shape functions are called *displacement differentiation functions*. Owing to the setup of the equation system in Eq. (8.20) and Eq. (8.21), the term displacement here also includes angular rotations. The shape functions depend on the chosen element type. In the case of a four-node quadrilateral plate element, the linear shape function for the respective nodes is given by

$$N_1 = \frac{1}{4}(1-\xi_1)(1-\eta_1) \tag{8.22}$$

$$N_2 = \frac{1}{4}(1+\xi_2)(1-\eta_2) \tag{8.23}$$

$$N_3 = \frac{1}{4}(1+\xi_3)(1+\eta_3) \tag{8.24}$$

$$N_4 = \frac{1}{4}(1-\xi_4)(1+\eta_4) \tag{8.25}$$

where ξ and η are the orthogonal bases of the local coordinate system of element [41]; see Fig. 8.2. The shape functions are valued at $N_m = 1$ at the respective node coordinates ξ_m and η_m for all element nodes $m = 1, \cdots, 4$, whereas all other functions are valued at zero.

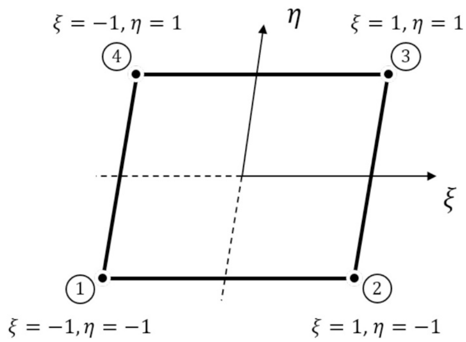

Fig. 8.2. Four-node quadrilateral element in the local - coordinate system with node coordinates

The partial differentials in Eq. (8.20) and Eq. (8.21) are calculated in the local coordinate system and result in the following values for integration at the respective corner nodes of the element [43]:

$$B_{local} = \begin{bmatrix} \frac{\partial N_1}{\partial \xi} & \frac{\partial N_2}{\partial \xi} & \frac{\partial N_3}{\partial \xi} & \frac{\partial N_4}{\partial \xi} \\ \frac{\partial N_1}{\partial \eta} & \frac{\partial N_2}{\partial \eta} & \frac{\partial N_3}{\partial \eta} & \frac{\partial N_4}{\partial \eta} \end{bmatrix} = \begin{bmatrix} -\frac{1}{2} & \frac{1}{2} & \frac{1}{2} & -\frac{1}{2} \\ -\frac{1}{2} & -\frac{1}{2} & \frac{1}{2} & \frac{1}{2} \end{bmatrix} \tag{8.26}$$

However, to apply the partial differentials of Eq. (8.26) according to Eq. (8.20) and Eq. (8.21), a transformation into the global coordinate system is necessary by using [43]

$$B_{global} = J^{-1} B_{local} = \begin{bmatrix} \frac{\partial N_1}{\partial x} & \frac{\partial N_2}{\partial x} & \frac{\partial N_3}{\partial x} & \frac{\partial N_4}{\partial x} \\ \frac{\partial N_1}{\partial y} & \frac{\partial N_2}{\partial y} & \frac{\partial N_3}{\partial y} & \frac{\partial N_4}{\partial y} \end{bmatrix} \tag{8.27}$$

with the Jacobian matrix J using the nonnormalized coordinates in the local ξ-η coordinate system

$$J = \begin{bmatrix} \frac{\partial x}{\partial \xi} & \frac{\partial y}{\partial \xi} \\ \frac{\partial x}{\partial \eta} & \frac{\partial y}{\partial \eta} \end{bmatrix} = \begin{bmatrix} \sum_1^m \frac{\partial N_m}{\partial \xi} x_m & \sum_1^m \frac{\partial N_m}{\partial \xi} y_m \\ \sum_1^m \frac{\partial N_m}{\partial \eta} x_m & \sum_1^m \frac{\partial N_m}{\partial \eta} y_m \end{bmatrix} \tag{8.28}$$

where x_m and y_m are the corner-related coordinates in the global coordinate system.The resulting element forces and coordinates exist in the global coordinate system. The hybrid approach allows a direct comparison of the approximated results with the FEM results when the same mesh is used. However, in the case of NASTRAN, the result output for element forces and moments is provided in the local coordinate system. The creation of the Jacobian matrix in Eq. (8.28) is required to use the local coordinates of the corner points to acquire the local elemental values during the calculation with the hybrid method. Accordingly, the nodal coordinates of the mesh used in the global coordinate system require a transformation into the local coordinate system. The matrix T used to perform transformations between the global and local coordinate systems is described by

$$T = \begin{bmatrix} e_{x,1} & e_{x,2} & e_{x,3} \\ e_{y,1} & e_{y,2} & e_{y,3} \\ e_{z,1} & e_{z,2} & e_{z,3} \end{bmatrix} \tag{8.29}$$

with the basis vectors $\vec{e}_i$ describing an element's local coordinate system axes in the global coordinate system [44]. To calculate the necessary $\vec{e}_i$, one requires a set of vectors $\vec{a}_{ik}$ describing the geometry of the element in the global coordinate system; see Fig. 8.3. The indices i and k describe the origin and destination nodes of the element, respectively.

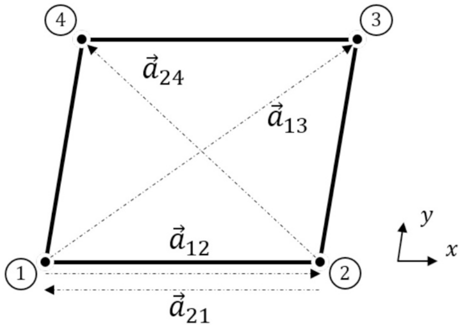

Fig. 8.3. Geometry describing element vectors for the transformation matrix built-up

By utilizing the column vectors $\vec{a}_{ik}$, one acquires the basis vectors that describe the transformation matrix by

$$\vec{e}_1 = \mathrm{norm}\left(\vec{a}_{13}\right) \tag{8.30}$$

$$\vec{e}_3 = \mathrm{norm}\left(\vec{a}_{13} \times \vec{a}_{24}\right) \tag{8.31}$$

$$\vec{e}_2 = \vec{e}_3 \times \vec{e}_1 \tag{8.32}$$

with the × -operator describing the cross-product of two vectors [44].

To align the local x-axis and local y-axis to the respective symmetry axes of the element, the local coordinate system requires rotation about the normal axis such that

$$T = \begin{bmatrix} \vec{e}_1 & \vec{e}_2 & \vec{e}_3 \end{bmatrix} R \tag{8.33}$$

The rotation matrix R describes the rotation about the normal axis for the angle α. Following the case of a rotation about the local z-axis

$$R = \begin{bmatrix} \cos(\alpha) & -\sin(\alpha) & 0 \\ \sin(\alpha) & \cos(\alpha) & 0 \\ 0 & 0 & 1 \end{bmatrix} \tag{8.34}$$

The rotation angle α is calculated by averaging the angles between the vector pairs $\left(\vec{a}_{12}, \vec{a}_{13}\right)$ and $\left(\vec{a}_{21}, \vec{a}_{24}\right)$ and is calculated via the dot product ($\bullet$) of a vector pairs by [44]

$$\alpha = -\frac{\cos\left(\vec{a}_{12} \bullet \vec{a}_{13}\right) + \cos\left(\vec{a}_{21} \bullet \vec{a}_{24}\right)}{2} \tag{8.35}$$

The resulting transformation matrix T in Eq. (8.33) transforms from the global coordinate system into the local coordinate system. The matrix requires a transposition to transform from the local coordinate system into the global coordinate system.

Data availability

Data will be made available on request.

References

[1] D. Noiseux, Measurement of power flow in uniform beams and plates, J. Acoust. Soc. Am. 47 (2) (1970) 238–247.
[2] G. Pavic, Measurement of structure borne wave intensity, Part I: Formulation of the methods, J. Sound Vib. 49 (2) (1976) 221–230.
[3] J. Verheij, Cross spectral density methods for measuring structure borne power flow on beams and pipes, J. Sound Vib. 70 (1) (1980) 133–139.
[4] R. Winter, M. Norambuena, J. Sinske, S. Zettel, High-resolution vibroacoustic characterization of DLR's Falcon 2000LX ISTAR aircraft, CEAS Aeronaut. J. 14 (2023) 953–963.
[5] G. Petrone, M. De Vendittis, S. De Rosa, F. Franco, Numerical and experimental investigations on structural intensity in plates, Compos. Struct. 140 (2016) 94–105.
[6] J. Arruda, P. Mas, Localizing energy sources and sinks in plates using power flow maps computed from laser vibrometer measurements, J Shock Vib. 5 (4) (1998) 235–253.
[7] A.A. Freschi, A. Pereira, K. Ahmida, J. Frejlich, J. Arruda, Analyzing the total structural intensity in beams using a homodyne laser doppler vibrometer, J. Shock Vib. 7 (2000) 299–308.
[8] J. Pascal, T. Loyau, X. Carniel, Complete determination of structural intensity in plates using laser vibrometers, J. Sound Vib. 161 (3) (1993) 527–531.
[9] J. Blotter, R. West, Identification of energy sources and sinks in plates by means of a scanning laser Doppler vibrometer, Noise Control Engineering 44 (2) (1996) 61–68.
[10] E. Williams, H. Dardy, R. Fink, A technique for measurement of structure borne intensity in plates, J. Acoust. Soc. Am. 78 (6) (1985) 2061–2068.
[11] T Loyau Pascal, J. Mann III, Structural intensity from spatial Fourier transformation and BAHIM acoustical holography method, in: *Proc. 3rd Int. Congress on Intensity Techniques, Senlis, France*, 1990, pp. 197–204.
[12] F. Pires, S. Avril, S. Vanlanduit, J. Dirckx, Structural intensity assessment on shells via a finite element approximation, J. Acoust. Soc. Am. 145 (1) (2019) 312–326.
[13] S. Zettel, M. Norambuena, R. Dewald, M. Böswald, Comparison of Laser doppler vibrometry and digital image correlation measurement techniques for applications in vibroacoustics, in: 29th International Congress on Sound and Vibration, Prague, Czech Republic, 2023, pp. 343–350.
[14] F. Egner, L. Sangiuliano, R. Boukadia, S. van Ophem, W. Desmet, E. Deckers, Polynomial filters for camera-based structural intensity analysis on curved plates, Mech. Syst. Sig. Process. 193 (15) (2023) 110245.
[15] S. Timoshenko, S. Woinowsky-Krieger, Theory of Plates and Shells, McGraw-Hill, New York, 1959.
[16] B. Lamarsaude, Y. Bousseau, A. Jund, Structural intensity analysis for car body design: going beyond interpretation issues through vector field processing, in: ISMA 2014, Leuven, Belgium, 2014, pp. 3677–3686.
[17] P. Groba, J. Ebert, T. Stoewer, C. Schaal, T. Melz, Detection of energy sinks and sources in the vibratory field of coupled structures with fluid-structure interaction, in: ISMA 2016, Leuven, Belgium, 2016, pp. 3945–3956.
[18] L. Sangiuliano, B. Reff, J. Palandri, F. Wolf-Monheim, B. Pluymers, E. Deckers, W. Desmet, C. Claeys, Low frequency tyre noise mitigation in a vehicle using metal 3D printed resonant metamaterials, Mech. Syst. Sig. Process. 179 (2022) 109335.
[19] K. Alfredsson, B. Josefson, M. Wilson, in: Use of the Energy Flow concept in Vibration Desing, American Institute of Aeronautics and Astronautics, 1996, pp. 1250–1255.
[20] J. Biedermann, R. Winter, M. Norambuena, M. Boeswald, A hybrid numerical and experimental approach for structural intensity analysis of stiffened lightweight structures, in: ISMA 2018, Leuven, Belgium, 2018, pp. 4101–4115.
[21] Y. Wang, R. Huang, Z. Liu, Using structural intensity approach to characterize vibro-acoustic behaviour of cylindrical shell structure, Coupled System Dynamics 7 (3) (2018) 297–319.
[22] Y. Ma, Q. Zhao, K. Zhang, M. Xu, W. Zhao, Effects of mount positions on vibrational energy flow transmission characteristics in aero-engine casing structures, J. Low Freq. Noise, Vib. Active Control 39 (2) (2020) 313–326.
[23] G. Petrone, A. Carzana, F. Ricci, S. De Rosa, Damage detection through structural intensity and vibration based techniques, Adv. Aircraft Spacecraft Sci. 4 (6) (2017) 613–637.
[24] M. Shepherd, S. Conlon, F. Semperlotti, S. Hambric, Structural intensity modeling and simulations for damage detection, J. Vib. Acoust. 134 (5) (2012) 051004.
[25] H. Lee, S. Lim, M. Khun, Diversion of energy flow near crack tips of a vibrating plate using the structural intensity techniques, J. Sound Vib. 296 (3) (2006) 602–622.
[26] G. Pavic, Vibrational energy flow in elastic circular cylindrical shells, J. Sound Vib. 142 (2) (1990) 293–310.
[27] R. Mindlin, Influence of rotatory inertia and shear on flexural motions of isotroplc elastic plates, J. Appl. Mech. 18 (1951) 31–38.
[28] L. Cremer, M. Heckl, B. Petersson, Structure-Borne Sound, Springer Verlag, Berlin Heidelberg, 2005.
[29] D. Gross, W. Hauger, P. Wriggers, Technische Mechanik, Springer Verlag, Heidelberg, 2014.
[30] N. Mandal, S. Biswas, Vibration power flow: a critical review, J. Shock Vib. 37 (1) (2005) 3–11.
[31] S. Hambric, Power flow and mechanical intensity calculations in structural finite element analysis, J. Vib. Acoust. 112 (4) (1990) 542–549.
[32] W. Maysenhölder, Körperschallenergie, Stuttgart/Leipzig: S. Hirzel, 1994.
[33] S. Buckert, Bewertung adaptiver Strukturen auf Basis der Strukturintensität, Darmstadt: TU Prints, Doctoral Thesis, 2013.

[34] A. Brandt, Noise and Vibration Analysis - Signal Analysis and Experimental Procedure, West Sussex, John Wiley & Sons Ltd, U.K., 2011.
[35] P. Langer, M. Maeder, C. Guist, M. Krause, S. Marburg, More than six elements per wavelength: the practical use of structural finite element models and their accuracy in comparison with experimental results, J. Comput Acoust. 25 (4) (2017) 1750025.
[36] A. Nashif, D. Jones, J. Henderson, Vibration Damping, Wiley-Interscience, New York, 1985.
[37] R. Horn, C. Johnson, Matrix Analysis, Cambridge, Cambridge University Press, U.K., 1985.
[38] R. Pascual, J. Golinval and M. Razeto, "A Frequency Domain Correlation Technique for Model Correlation and Updating," *International Modal Analysis Conference, Orlando, Florida,* pp. 587-592, 1997.
[39] J. Mottershead, M. Link, M. Friswell, The sensitivity method in finite element model updating: a tutorial, Mech. Syst. Sig. Process. 25 (2011) 2275–2296.
[40] P. Welch, The use of fast Fourier transform for the estimation of power spectra: a method based on time averaging over short, modified periodograms, IEEE Trans. Audio Electroacoust. 15 (2) (1967) 70–73.
[41] M. Petyt, Introduction to finite element vibration analysis, Cambridge, Cambride University Press, U.K., 1990.
[42] M. Link, Finite Elemente in der Statik und Dynamik, Springer Vieweg, Wiesbaden, 2014.
[43] M. Okereke, S. Keates, Finite Element Applications, Springer, Cham, Switzerland, 2018.
[44] MSC Software Coorporation, "MSC Nastran 2018.2 - Reference Guide," USA, 2018.